3D printed microneedle patches using stereolithography (SLA) for intradermal insulin delivery

Economidou, S. N., Pere, C. P. P., Reid, A., Uddin, M. J., Windmill, J. F. C., Lamprou, D., & Douroumis, D. (2019). 3D printed microneedle patches using stereolithography (SLA) for intradermal insulin delivery. *Materials Science and Engineering C: Materials for Biological Applications*. https://doi.org/10.1016/j.msec.2019.04.063

Document Version:
Peer reviewed version

Queen's University Belfast - Research Portal:
[Link to publication record in Queen's University Belfast Research Portal](#)

3D printed microneedle patches using stereolithography (SLA) for intradermal insulin delivery

AUTHOR NAMES

Sophia N. Economidou[1], Cristiane Patricia Pissinato Pere[1], Andrew Reid[2], Md. Jasim Uddin[3], James F.C. Windmill[2], Dimitrios A. Lamprou[4]*, Dennis Douroumis[1]*

AUTHOR ADDRESS

[1]Medway School of Pharmacy, University of Kent, Medway Campus, Central Avenue, Chatham Maritime, Chatham, Kent ME4 4TB, United Kingdom

[2]Centre for Ultrasonic Engineering, Department of Electronic and Electrical Engineering, University of Strathclyde, 204 George St, Glasgow, G1 1XW, Scotland, United Kingdom

[3]Department of Pharmacy, BRAC University, Bangladesh. Address: 41 Pacific Tower, Mohakhali, Dhaka-1212, Bangladesh.

[4] School of Pharmacy, Queen's University Belfast, 97 Lisburn Road, Belfast, BT9 7BL, United Kingdom

18

19   Abstract

20   **3D printed microneedle arrays were fabricated using a biocompatible resin through**

21   **stereolithography (SLA) for transdermal insulin delivery. Microneedles were built by**

22   **polymerising consecutive layers of a photopolymer resin. Thin layers of insulin and sugar**

23   **alcohol or disaccharide carriers were formed on the needle surface by inkjet printing. The**

24   **optimization of the printing process resulted in superior skin penetration capacity of the**

25   **3D printed microneedles compared to metal arrays with minimum applied forces varying**

26   **within the range of 2 to 5N. Micro–CT analysis showed strong adhesion of the coated films**

27   **on the microneedle surface even after penetration to the skin. *In vivo* animal trials revealed**

28   **fast insulin action with excellent hypoglycaemia control and lower glucose levels achieved**

29   **within 60 min, combined with steady state plasma glucose over 4 h compared to**

30   **subcutaneous injections.**

31

32   Introduction

33   Transdermal Drug Delivery (TDD), the ability to effectively convey drugs through the human

34   skin, is an appealing concept, aiming at surpassing the pitfalls of the traditional administration

35   routes. The broader adoption of the transdermal route, however, is hampered by restrictions that

36   stem from the nature of the skin barrier itself, especially by the stratum corneum. Microneedles

37   (MNs) are small devices that can pierce this outermost, most impermeable layer of the human

38   skin and successfully deliver active substances such as drugs, Ribonucleic acid (RNA),

39   Deoxyribonucleic acid (DNA), and vaccines straight into the dermal microcirculation [1–4] .

40   Due to their small size they leave skin nerves intact upon insertion [5], while they increase

41 bioavailability since the drug does not pass through any metabolic systems [6]. The MN-

42 mediated drug delivery is realised through multiple strategies that employ solid, coated, hollow,

43 hydrogel-forming and soluble MNs [7].

44 Since their introduction over 20 years ago, MN systems have attracted significant attention for

45 their potential to replace traditional drug administration routes. In the field of diabetes type 1 and

46 some types of type 2, the vast majority of patients rely on subcutaneous needle injections for

47 insulin replacement, a treatment approach highly associated with reduced patient-compliance [8].

48 Pain, skin thickening due to recurring injections, needle phobia and insulin leakages on the skin

49 surface [9,10] have motivated vigorous research on MN-based systems for transdermal insulin

50 delivery.

51 Recent advances encompass the use of moulding techniques for the development of insulin-

52 loaded dissolvable MN systems. Wang *et al.* introduced a bioinspired MN system consisting of

53 dissolvable cross-linked poly(vinyl alcohol) (PVA) gel, catalase and glucose oxidase (GOx) that

54 responds to high glucose conditions by releasing insulin to the circulation. *In vivo* tests showed

55 that the systems were effective in maintaining normal blood glucose levels [11]. In another

56 study, modified alginate and hyaluronate were combined into a dissolvable, insulin-

57 encapsulating MN system. The MN arrays demonstrated good mechanical properties and skin

58 penetration capability while clinical studies demonstrated that the MNs almost fully dissolved

59 into the skin. The released insulin achieved a sustained hypoglycaemic effect and good relative

60 bioavailability of insulin, compared with subcutaneous injections [12]. Similar results in terms of

61 mechanical properties, relative insulin bioavailability and pharmacological activity were also

62 obtained by a study that manufactured composite dissolvable MNs [13]. The forenamed studies

63   demonstrate that MN can be a promising alternative to subcutaneous injections for insulin

64   therapy.

65   Nonetheless, there are several hampering parameters that need to be taken under consideration

66   for the development of transdermal insulin delivery systems. The first relates to the time needed

67   for the detection of the drug into the systemic circulation; dissolvable systems are highly

68   dependent on the dissolution rate of the materials encapsulating the drug and may not be suitable

69   for fast insulin administration. To circumvent that issue, Ross *et al*. developed a solid MNs-

70   based system, coated with insulin-containing formulations through inkjet printing [14]. The use

71   of this technology permitted the accurate deposition of uniform and homogeneous coatings, with

72   high reproducibility. The implementation of inkjet printing for the development of thin layers on

73   the microneedle surface resulted in rapid insulin release within the first 20 min.

74   Another pitfall stems from the use of moulding techniques, that involve a series of multiple,

75   often time-consuming steps. It is evident, that the upscaling of such processes can be

76   challenging. Furthermore, there is a lack of clinical data related to cytotoxicity of materials used

77   for moulded microneedles which actually limits their applications. Another important

78   disadvantage is the limited drug loading in polymeric microneedles without affecting their

79   mechanical properties and piercing capacity. In order to circumvent this issue several authors

80   proposed the use of large patches which in turn results in difficulties to apply the arrays in a

81   uniform manner and subsequently in dose variation of the administrated substances. Recently,

82   efforts have been made on the integration of the revolutionary technology of 3D printing as a

83   manufacturing method for MN-based systems. 3D printing or Additive Manufacturing (AM) is a

84   family of technologies that implement layer-by-layer processes to fabricate physical models,

85   based on a Computer Aided Design (CAD) model. 3D printing permits the fabrication of high

86 degrees of complexity with great reproducibility, in a fast and cost-effective fashion [15–18]. In

87 the field of transdermal drug delivery systems, the use of photopolymerization-based techniques

88 such as Stereolithography (SLA), Digital Light Processing (DLP) and Two-Photon-

89 Polymerization (2PP) for the development of MNs has been reported [19–22]. Gittard *et al.*

90 fabricated MNs of various geometries for wound healing applications using a DLP system. The

91 MNs were then coated with silver and zinc oxide thin films by pulse laser deposition and their

92 antimicrobial character was verified [23]. In another study, drug-loaded MNs were developed

93 when a skin anticancer drug was incorporated into the photo-sensitive polymer blend prior to

94 photopolymerization through a micro-stereolithographic (DLP) apparatus [24].

95 In this study, 3D printed MN arrays featuring two different MN designs, pyramid and spear,

96 were developed employing a commercial SLA printer and a biocompatible Class 1 polymer. The

97 3D printed arrays were subsequently coated with insulin–sugar films using inkjet printing.

98 Mannitol, trehalose and xylitol were used as insulin carriers to preserve insulin activity prior to

99 the deposition of active films on the MNs surface. *In vitro* and *in vivo* studies demonstrated rapid

100 insulin release from the coated MN systems. The usage of SLA for 3D printing of microneedle

101 arrays is anticipated to overcome the existing disadvantages of conventional techniques by

102 providing high precision, rapid fabrication, reduced processing steps and freedom to print a wide

103 range of shapes.

104 Materials and methods

105 Materials

106 The insulin employed in this study was bovine and was procured in a 10 mg mL^{-1} solution from

107 Sigma-Aldrich (Gillingham, UK). Xylitol (Xylisorb® 90) and mannitol (Pearlitol®) were

108 donated by Roquette Freres (France) while trehalose dihydrate was bought from Sigma-Aldrich

109 (Gillingham, UK). The resin used to fabricate the MNs was the biocompatible Class I resin,

110 Dental SG, by Formlabs. Streptozocin (≥75% α-anomer basis, ≥98%) and citric acid were both

111 purchased from Merck Chemical Co. (Darmstadt, Germany). All solvents were of analytical

112 grades.

113

114 Additive manufacturing of microneedles

115 The MN arrays were designed using an engineering software (SolidWorks, Dassault Systems) as

116 patches of 15x15x1 mm. The patches featured two different needle shapes, a pyramid and a flat

117 spear shaped that geometrically resembled the shape of metallic MNs that has been studied

118 elsewhere [16]. This design, named 'spear' in the framework of this study, had base dimensions

119 of 0.08x1 mm, while the dimensions of the base for the pyramid MN were 1x1 mm. The length

120 of all MNs was 1 mm and all patches had a 6x8 needle layout, yielding 48 MNs per patch. The

121 arrays were 3D printed using the Form 2 SLA printer by Formlabs with high resolution

122 capabilities (25 and 140 microns for z and x axes, respectively). After fabrication, the arrays

123 were washed in isopropyl alcohol bath to remove unpolymerized resin residues and then cured

124 for 60 min at 40 °C under UV radiation using the MeccatroniCore BB Cure Dental station.

125 Coating of microneedles through inkjet printing

126 An inkjet printer was employed (NanoPlotter II, Gesim, Germany) to print thin insulin-sugar

127 films on the surface of the 3D printed MNs. The inkjet printer forms the drug-containing films

128 depositing multiple layers of insulin – sugar droplets on each microneedle using a piezo-driven

129 dispenser (PicPip 300). In each coating cycle (layer), the dispenser jetted 2 droplets of

130 formulation in 10 spots along each needle's longitudinal axis. A total of 92 coating cycles

131 resulted in a 10 UI (350 µg) of insulin per array. The coated arrays were then incubated at room

132 temperature for 24 hours to allow the evaporation of the solvent (de-ionised water) and the

133 formation of uniform films. For the purposes of this study three coating formulations were used,

134 consisting of insulin:xylitol (5:1 wt/wt), insulin: mannitol (5:1 wt/wt) and insulin:trehalose (5:1

135 wt/wt) as 2% solid content. Prior to the coating process, the arrays were mounted on a metal stub

136 at 45° relative to the dispenser, while its tip (50 µm) was placed close to the MN surface to avoid

137 losses of material.

138 Scanning electron microscopy (SEM)

139 The coated MN arrays were mounted onto aluminium stubs using a double-sided carbon

140 adhesive tape (Agar Scientific, UK). Each coated MN array was examined by SEM (Hitachi SU

141 8030, Japan) using a low accelerating voltage (1.0kV). A low accelerating voltage was used to

142 avoid electrical charges on the MNs. The images of coated MNs were captured digitally from a

143 fixed working distance (11.6 mm) using different magnifications (e.g. 30, 80, 110 or 120 x).

144 X-Ray Computer Micro Tomography

145 X-Ray Micro Computer Tomography (µCT) scans were performed on coated 3D printed

146 pyramid MN. The equipment employed was a Bruker Skyscan 1172, with an SHT 11 Megapixel

147 camera and a Hamamatsu 80kV (100µA) source. The samples comprised of 3D printed pyramid

148 MN coated with the three insulin/sugar formulations; Sample A: insulin:xylitol (5:1 wt/wt),

149 Sample B: insulin: mannitol (5:1 wt/wt) and Sample C: insulin:trehalose (5:1 wt/wt). After the

150 scans of the coated arrays were performed, the arrays were inserted in 8-ply strips of parafilm,

151 applying a force of 5 N, to examine the performance of the coating during piercing and to

152   investigate whether any coating material will remain on the parafilm surface, causing drug

153   losses. Moreover, the penetration depth was measured. The samples were mounted vertically on

154   a portion of dental wax and positioned 259.4 mm from the source. No filter was applied to the X-

155   Ray source and a voltage of 80 kV was applied for an exposure time of 1,050 ms. The images

156   generated were 2,664 x 4,000 pixels with a resolution of 6.75 μm per pixel.

157   A total of 962 images were taken in 0.2º steps around one hemisphere of the sample with the

158   average of 4 frames taken at each rotation step. The images were collected and a volumetric

159   reconstruction of the sample generated by Bruker's *CTvol* software. The threshold for this

160   attenuation signal was set manually to eliminate speckle around the sample, and then further

161   cleaned with a thresholding mask using Bruker's *CTAn* software. The images produced by the

162   μCT are based on the level of attenuation though the sample, which is dependent on the

163   thickness of the material and its absorption coefficient. Here, it is assumed that the absorption

164   coefficient is linearly proportional to the density of the material and the resulting densities

165   expressed in Hounsfield Units (HU), with -1000 being the density of air and 0 being the density

166   of water.

167   Circular Dichroism (CD)

168   Insulin solution and the respective solutions of the insulin-sugar films were diluted to 1.0 mg

169   mL^{-1} in deionised water and the spectra were recorded at 20 ºC between 190 and 260 nm by CD

170   (Chirascan, Applied Photophysics, UK) using a 0.1 mm polarization certified quartz cell

171   (Hellma). Spectra were recorded using a step size of 1 nm, a bandwidth of 1 nm and an

172   acquisition time of 1 sec. Four scans were recorded for each sample, averaged and a

173   corresponding spectrum of water was subtracted from each spectrum. For estimation of the

174   secondary structural composition of insulin, the CD spectra were evaluated using the CD SSTR

175   method [25].

176   Raman Spectroscopy

177   The films and their respective components were analysed using Raman microscopy (Jobin Yvon

178   LabRam I) with a laser of 532 nm wavelength coupled with an optical microscope with 50x

179   objective.

180   Penetration studies through porcine skin

181   The effect of the MN geometry on the force required to pierce the skin has been documented

182   [26]. In this study, to determine the effect of needle shape on the force required for skin

183   penetration, piercing tests using porcine skin were conducted. Identical piercing tests were

184   carried out using metallic MN arrays that have been studied and are described in literature [16],

185   to maintain a frame of reference with the respective studies. A texture analyser was employed,

186   and the MN array was mounted on the moving probe using double-sided adhesive tape. Prior to

187   testing, the porcine skin samples were placed in waxed petri dishes. Continuous force and

188   displacement measurements were recorded to identify the point of needle insertion. The speed of

189   the moving probe was 0.01 mm s^{-1}.

190   Axial force mechanical testing of MNs

191   To evaluate the mechanical behaviour of the 3D printed microneedles, fracture testing under

192   axial loading was performed. The arrays were fixed onto a metal plate and were pressed against a

193   flat metal block attached to the moving head of a Tinius Olsen testing machine, until a pre-set

194   displacement of 500 μm (height/2) was reached. Continuous force and displacement

195   measurements were recorded to identify the point of needle failure. The speed of the moving

196   probe was 1 mm/s and the experiments were replicated 5 times for each design.

197   Preparation of porcine skin for in vitro release of insulin

198   The release of insulin from the coated MNs through abdominal porcine skin was studied using

199   Franz diffusion cells (PermeGear, Inc., PA, USA). The full thickness abdominal porcine skin

200   was collected from a local slaughterhouse (Forge Farm Ltd, Kent, UK) and was then shaved

201   using a razor blade. The fatty tissue below the abdominal area of porcine skin was removed with

202   scalpel and then pinned onto polystyrene block and wiped with 70 % ethanol. The skin was then

203   cut by applying the dermatome at an angle of ±45° (Padgett dermatome, Integra LifeTMSciences

204   Corporation USA). The thickness of the skin was measured by using a calliper and the tissue

205   disks of the required dimensions were cut for the Franz diffusion cells using a scalper. The skin

206   tissue (1.0 ± 0.1 mm thick) was placed onto filter paper soaked in a small amount of saline

207   phosphate buffer (pH 7.4) for 2 h.

208   In vitro release of insulin through porcine skin

209   A total diffusion area of 1.1 cm^2 was used to assess the insulin release. The MN arrays were

210   inserted into the abdominal porcine skin samples for 30 s, via manual finger pressure. The

211   sample was then mounted onto the donor compartment of a Franz diffusion cell. The temperature

212   of the Franz cells was maintained at 37ºC using an automated water bath (Thermo Fisher

213   Scientific, Newington, USA). Sample fractions (6-6.5 mL h^{-1}) were collected using an auto-

214   sampler (FC 204 fraction collector, Gilson, USA) attached to the Franz diffusion cells system.

215   Statistical analysis for the drug release was performed by using a Mann-Whitney nonparametric

216   test and t-test analysis for the in vivo studies (InStat, GraphPad Software Inc., San Diego, CA,

217   USA), where samples were considered as statistically significant at $p < 0.05$.

218   High-Performance Liquid Chromatography (HPLC)

219   The amount of insulin collected from the receptor fluid was determined by HPLC (Agilent

220   Technologies, 1200 series, Cheshire, UK) equipped with a Phenomenex Jupiter 5u c18 300 Å,

221   LC Column (250×4.60 mm, particle size 5 μm, Macclesfield, UK). The mobile phase consisted

222   of water with 0.1 % Trifluoroacetic Acid (TFA) and acetonitrile with 0.1% TFA (66:34v/v), with

223   a 1 mL min^{-1} flow rate. The column was equilibrated at 35°C, the injection volume was 20 μL

224   and the eluent was analysed with a UV detector at 214 nm. The results were integrated using

225   Chemstation® software and the samples analysed in triplicates.

226   In vivo release in diabetic mice

227   Prior to the induction of diabetes, Swiss albino female mice (120 ± 10 g) were allowed free

228   access to solid bottom cages with controlled diet and water for 3 days. Mice were subcutaneously

229   injected on the flank with streptozotocin (70 mg kg^{-1}) in citric acid buffer (pH 4.5) to produce a

230   diabetic animal model. To confirm the induction of diabetes, the fasting blood glucose level was

231   measured at scheduled times using a one-touch glucometer (ACCU-CheckVR Active, Roche,

232   Germany). After one week, mice with blood glucose exceeding 300 mg/dl were considered as

233   diabetic. The diabetic animals were anesthetised and shaved carefully using an electric razor

234   (Panasonic, USA) 24 hours prior to the experiments. Furthermore, the diabetic mice were fasted

235   for 12 hours before the beginning of the study, receiving only water and libitum. The mice were

236   randomly divided into three groups (n=3 for each group): (1) untreated group as negative

237   control; (2) subcutaneous injection (SC; 0.2 IU/animal) as positive control; (3) 3D printed MN

238   (0.2 IU/array). The 3D printed MN arrays were applied onto the dorsal skin of the animals using

239   adhesive tape (3M, USA) to prevent any dislodgement during therapy. After 2 hours, the 3D

240   printed MN patches were removed. For all groups, blood samples were collected from the

241   jugular vein at 0, 1, 2, 3 and 4 hours after the insulin administration and the blood glucose level

242   was measured using the glucometer mentioned. Plasma insulin concentrations were measured via

243   an insulin-EIA Test kit (Arbor Assays, MI, USA). The treatment strategy is described in Table 1.

244   All animal experiments throughout this study were approved by the Research Ethics Committee

245   (reference number 0003/17, Department of Pharmacy, Southern University Bangladesh) and

246   conducted according to the Southern University Bangladesh policy for the protection of

247   Vertebrate Animals used for Experimental and Other Scientific Purposes, with implementation

248   of the principle of the 3Rs (replacement, reduction, refinement). No skin reactions to MNs

249   occurred.

250   Pharmacodynamic and pharmacokinetic profile of insulin-coated 3D printed MNs

251   The minimum glucose level (Cmin) and the time point of minimum glucose level (Tmin) were

252   calculated from the plasma glucose level versus time curve. The relative pharmacological

253   availability (RPA) was calculated using equation 1.

254   RPA(%) = (AAC3DMN×dosesc)/ (AACsc× dose3DMN) × 100   (Eq.1)

255   Where AAC3DMN indicates the area above the curve after the application of the insulin-coated

256   3D printed MNs, and AACsc shows the area above the curve after the subcutaneous injection of

257   insulin.

258   The maximum plasma insulin concentration (Cmax) and the time point of maximum plasma

259   insulin concentration (Tmax) were calculated from the plasma insulin concentration (µIU/ml)

260   versus time curve. The relative bioavailability (RBA) was determined using equation 2.

261   RBA(%)=(AUC3DMN × dosesc)/ (AUCsc × dose3DMN) × 100   (Eq.2)

262   Where AUC3DMN indicates the area under the curve after the application of the insulin-coated

263   3D printed MNs, and AUCsc shows the area under the curve after the subcutaneous injection of

264   insulin.

265   Results and Discussion

266   Additive Manufacturing and printability of microneedles

267   MN arrays featuring pyramid and spear needles were 3D printed using a commercial SLA printer

268   based on digital CAD designs developed via appropriate engineering software. The polymer

269   employed was a photo-sensitive Class I resin which has been FDA approved. All arrays were

270   washed and subsequently cured under UV radiation in a controlled temperature environment to

271   improve the material's mechanical performance.

272   The capability of 3D printing technology to manufacture complex structures reproducibly and

273   accurately in a one-step-fashion, was exploited in this work to build different designs of MN

274   arrays. Although the degree of complexity that can be achieved through 3D printing is often not

275   achievable through many conventional techniques of MN manufacturing, the technology is

276   hampered by restrictions in terms of resolution that can affect the formation of sharp MN tips.

277   Conventional low-budget SLA printers have a maximum resolution of 100 microns that is

278   governed by the size of the laser focal point and restricts the minimum size of MN tip that can be

13

279 formed. The MNs designed in the framework of this study featured a tip of 100 microns by

280 design and their penetration capability through porcine skin was tested to verify that they will

281 successfully and painlessly pierce the skin.

282 The printability of MNs was further improved when printing-in-an-angle was implemented,

283 leading to finer, sharper MN tips. An innate characteristic of the SLA technology is the

284 interdependence between the print quality and the cross-sectional area in the z-axis; the smaller

285 the z-axis cross-sectional area, the better the quality. This stems from the peel-off function of the

286 printing process, according to which, after the completion of each layer, a wiper slides and peels

287 the structure off the bottom of the resin tank. Larger z-axis cross sectional areas lead to greater

288 forces applied by the wiper, which can deform the printed structures. Orienting the part to

289 minimise the contact area of the structure to the resin tank avoids the possible distortions during

290 the peel-off process and leads to better print quality.

291 SLA parts are considered mechanically isotropic which ensures the mechanical properties of the

292 arrays are not affected by the angle of printing. In addition, an influential factor of the

293 mechanical performance of the MN arrays is the selection of post-process curing parameters

294 (time and temperature). Further research is required to determine the effect of those factors on

295 the overall mechanical and piercing behaviour of the MN arrays. In this work, the MNs were

296 cured in a UV chamber for 60 min in temperature of 40 ºC. It is demonstrated in this study that

297 those parameters yielded systems that successfully pierced through porcine skin requiring small

298 forces, with no needle failure occurring.

299 As discussed above due to technical limitations of the existing MN manufacturing techniques

300 (e.g. moulding, lithography) such as limited drug loading, dose consistency and scalability issues

301 there are no commercialized products. Polymeric MNs are fabricated using moulding approaches

302 while metal MNs implement dip – coating techniques which renders both approaches impractical

303 for large scale manufacturing. In contrast scale-up of SLA printed MNs is directly related to the

304 usage of large volume printers or the in-line arrangement of existing printers. We envisage that

305 the implementation of SLA printed MNs will open new horizons for transdermal drug delivery

306 due to the low cost of the printers, printing inks and fast fabrication times.

307 SEM analysis demonstrated that through the use of the SLA technology, uniform and

308 reproducible arrays were developed (Fig. 1a,b). In Fig. 1, the high consistency and

309 reproducibility of the MN layers is depicted, and the formation of sharp tips is demonstrated. It is

310 evident, that the high-resolution capabilities of the printer allowed the parallel fabrication of

311 identical and reproducible arrays with characteristics that favour the skin insertion.

312 Coating of microneedles through inkjet printing

313 Insulin and sugar alcohol coatings were formed on the surface of the 3D printed MNs using

314 inkjet printing and a piezoelectric dispenser. A similar process was developed in earlier studies

315 for coating metallic MNs [16,27], where the applied voltage (mV) and pulse duration (ms) were

316 tuned to achieve the production of droplets of 300 pL volume with particle size of 100-110 μm.

317 Fig. 1c,d illustrates the uniformity and reproducibility of the coatings on the MN surface without

318 any losses of material in the form of satellite droplets on the substrate. Moreover, it is

319 demonstrated that the consecutive jetting cycles produced drug-containing films that are smooth

320 and level in comparison to other techniques such as dip coating that may yield voluminous and

321 inconsistent coatings. This smooth morphology of the films prevents the losses of drug during

322 MN insertion that occur when bulky coatings remain on the skin surface.

323 The drug carriers selected were two alcohol sugars (xylitol, mannitol) and a disaccharide

324 (trehalose). Those excipients have been reported to favour the immediate coating dissolution in

325 the skin and to enhance insulin stability in solid state [28–30] .

326 X-Ray Computer Micro Tomography

327 The coated 3D printed pyramid MN arrays were scanned using the Bruker Skyscan 1172 and an

328 overview of the array is presented in Fig. 2a. For sample A, an average needle base area of 1.095

329 mm^2 and an average needle height of 1.034 mm were measured. For samples B and C, the

330 average needle base areas were measured as 1.065 mm^2 and 1.091 mm^2 and the average needle

331 heights as 1.040 mm and 1.038 mm, respectively. The average interspacing of the pyramids

332 between the centre points was 1.842 mm, 1.865 mm, and 1.864 mm between columns, and 1.788

333 mm, 1.810 mm, and 1.796 mm between rows for samples A, B and C respectively. Scans taken

334 from the left-hand side of the arrays illustrate the thin coating films fabricated through inkjet

335 printing, in comparison with respective ones taken from the back side of the array (Fig. 2b,c).

336 The relative density of the MNs relative to the control sample (uncoated 3D printed pyramid

337 MNs) showed an increase of approximately 200 HU between all coated samples and the control

338 (Fig. 3a,b). Profile lines across a row of MNs revealed a coffee-ring effect in the density of the

339 coating material deposition. While denser material was distributed randomly within each of the

340 MNs, a fringe layer of 10-15 μm was apparent with the effect being most pronounced in the

341 insulin:xylitol coated sample (Fig. 3c).

342 Penetration experiments in 8-ply strips of parafilm were performed applying a 5 N force (Fig. 4).

343 The penetration depth was measured as 559 μm, 662 μm and 650 μm for samples A, B and C,

344   respectively. The μCT scans illustrate that the coating stays on the MN surface throughout the

345   piercing process and there is no material remaining on the parafilm surface.

346   Circular Dichroism

347   Circular dichroism (CD) spectroscopy is a reliable technique for the evaluation of the secondary

348   structure of proteins in a solution. The influence of the two polyols and the disaccharide on

349   insulin molecule as well as their interactions were studied using CD and the estimation of insulin

350   secondary structure was performed by CDSSTR method [31,32].

351   The far-UV CD spectra of insulin and insulin-sugar films (Fig. 5a) were found to be coincident

352   with the one of standard insulin solution, showing double minima around 210 and 222 nm which

353   are typical of predominant α-helix structure proteins as already reported elsewhere [28,33–35].

354   However, a slight decrease in Molar ellipticity is noted when insulin solution is dried which is

355   also supported by the decrease of the estimated percentage of α-helix and increase of the β-sheet

356   content. Such behaviour may be indicative of the unfolding tendency of insulin during

357   dehydration [36]. Interestingly, once the sugars were added, all the respective insulin-sugar films

358   spectra showed higher Molar intensities than the insulin film alone, indicating an increase in the

359   α-helix content. The protective property of those sugars can be explained by the water

360   replacement mechanism which proposes that sugars may maintain the three-dimensional

361   structure of proteins by hydrogen-bonding with them [37,38]

362   Among the tested sugars, xylitol presented the best capability to maintain insulin in its native

363   secondary structure with even higher amounts of α-helix content. The reason for this still remains

364   unclear and further research is needed.

365   Raman Spectroscopy

366   In this work, the Raman spectrum of native insulin shows a strong peak at 1661 cm^{-1} due to the

367   amide I mode of α-helix structure and a shoulder at 1682 cm^{-1} which is attributed to random coil

368   form as previously reported by Yu et al. [40]. Distinctive peaks of sugars were not found in

369   Raman mainly because insulin was 5 times more concentrated than the sugars in the films.

370   Likewise, the amorphous nature of the dried formulation (XRD analysis - data not shown) is

371   unlikely to afford a strong Raman signal.

372   Overall, insulin-sugar formulations showed similar Raman spectra to the native insulin (Fig. 5b).

373   Nonetheless, a slight shift in amide I band position can be seen for all formulations. Amide I

374   band of insulin-xylitol and insulin-mannitol formulations was shifted towards greater frequency,

375   1663 cm^{-1} and 1662 cm^{-1}, respectively, while insulin-trehalose band was shifted to lower

376   frequency at 1658 cm^{-1}. Those events were also reported by Carpenter and Crowe [37] and

377   Souillac et al. [41], who described that those changes might be due to the different effect of each

378   sugar on the vibrational spectra of insulin as well on the hydrogen bonding and couplings

379   between the adjacent peptide units.

380   Many researchers have investigated the protective properties of different sugars on polypeptides,

381   proteins and biomolecules [42–44]. It has been advocated that protein aggregation and

382   denaturation can be prevented by using carbohydrates as protectants. Protein protection by the

383   sugars in a dried system can be explained by the water replacement mechanism which suggest

384   the sugars may substitute water molecules around the biomolecules of proteins, maintaining its

385   three-dimensional structure by providing sites with hydrogen-bonding species [37,45,46].

386   Zeng *et al.* studied the impact of relative humidity (RH) on dehydration of insulin crystals and

387   they found the hydration water from insulin crystal can be gradually excluded when the RH is

18

388 decreased. They used the high frequency region in Raman spectroscopy to access the band at

389 ~3450cm^{-1} which is caused by both water and amino acid residues with O-H groups. A

390 continuous dropping of the O-H stretching band around 3450 cm^{-1} was observed while the RH

391 was reduced, indicating dehydration of the molecule [47].

392 From Fig. 5b it can be seen that for all formulation the S-S vibration bands are located close to

393 513 cm^{-1} suggesting that all disulphide bonds are in an adopted more stable gauche – gauche -

394 gauche conformation [47,48] as a result of the complete water removal during inkjet printing.

395 Tyr residues present Raman peaks at 642, 828, 852, and 1174 cm^{-1}, while the 1206 cm^{-1} peak is

396 related to both Tyr and Phe residues. Furthermore, the ratios of $I_{852/I828}$ and $I_{1174/I1206}$ varied from

397 0.91 – 1.02 and 0.77 – 0.81 respectively.   These values are much lower compared to those

398 observed from Zeng et al. [47], for insulin crystals at very low RH (2%). This phenomenon

399 suggests significant water loss of the coated formulation and stronger H – bonding interactions.

400 Vibrational modes in the area of 1100 – 1300 cm^{-1} have shown to be sensitive to the changes of

401 hydrogen bonds which involve the phenolic hydroxyl groups of Tyr residues and particularly the

402 $\nu_{7á}$ frequency. In Fig. 5b the $\nu_{7á}$ has a frequency of 1275cm^{-1} which is a robust evidence that the

403 phenolic OH group of Tyr is strongly hydrogen bonded to a base atom [49].

404 Penetration studies through porcine skin

405 The 3D printed pyramid and spear shaped MN arrays were tested for their porcine skin

406 penetration capability using a texture analyser. Identical experiments were performed using

407 metallic MNs and the results were compared to the respective ones obtained from the 3D printed

408 MN experiments. All piercing tests were successful with no MN damage or failure. Throughout

409 each test, measurements of force and displacement were taken (Fig. 6a).

410   All curves presented an initial linear segment (displacement < 0.3 mm); after that, the slope was

411   changing constantly until a maximum force value was reached and a steep decrease of the force

412   was observed. This value is identified as the maximum force required for MN insertion [26]. The

413   non-linear behaviour of the force-displacement curve indicates that the process of MN insertion

414   to the skin is comprised of small penetrations where the MNs gradually tear the skin, before the

415   load reaches the maximum value that makes the insertion abrupt [50]. The maximum force

416   required for the MNs to successfully pierce the skin plays a crucial role when different MN

417   designs need to be compared. As presented in Fig. 6b, the pyramid MN required the least amount

418   of force to penetrate the porcine skin.

419   Axial force mechanical testing of MNs

420   The two studied MN designs were tested under compressive axial loading to determine the force

421   of microneedle fracture as a function of geometry. The force vs displacement measurements and

422   respective fracture strength values are presented in Fig. 7.

423   The two designs exhibited different mechanical behaviours during testing. For both designs, the

424   recorded force increased until the ultimate load was reached, and fracture occurred. For the spear

425   MNs, the point of fracture appears as a peak at approximately 175 N, followed by a drop of the

426   recorded load; as the MNs were kept being pressed against the metal block after fracture, the

427   load was considerably decreased. On the contrary, the pyramid geometry showed a discontinuity

428   at approximately 457 N which is identified as the point of initial needle failure. Afterwards, the

429   load kept increasing as the microneedles kept being compressed. This difference in mechanical

430   behaviour is attributed to the different modes of needle failure. On the one hand, the spear MNs

431   fractured in the lateral direction, perpendicular to the loading axis, a finding that was confirmed

432   by visual observation. This mode of failure was expected, due to the small thickness of the MNs

433   in that direction, which translates to minimisation of area, thus increased stress fields. On the

434   other hand, the pyramid MNs failed under pure compression, with the tip failing first and

435   additional, increasing force required for the compression of the remaining MN body. These

436   findings verify that both designs are safe for application since the fracture strengths of the arrays

437   are far greater than the respective forces needed for needle penetration through porcine skin.

438   They also confirm that the pyramid geometries present the best potential between the two studied

439   designs.

440   In vitro release of insulin through porcine skin

441   The in vitro insulin release studies from 3D printed pyramid and spear MNs were investigated

442   using porcine skin in Franz cells. The used carriers, mannitol, trehalose and xylitol not only

443   preserved insulin in its native form but also provided fast dissolution rates. As shown in Fig.

444   8a,b for the pyramid designs approximately 80% of insulin was released in the first 2 min with

445   86 – 92% within 8 min. The rapid release profiles were obtained for all insulin carriers and no

446   statistical difference was observed (two-tail p = 0.0021).

447   The coating of each pyramid side resulted to higher surface area exposed for hydration and thus

448   faster hydration rates. In contrast, the spear 3D printed designs presented slightly slower insulin

449   release rates with 62 – 70% and 81 – 84% released within 2 min and 8min respectively. Overall,

450   the rapid insulin release rates of the 3D printed MNs was attributed to the hydrophilic nature of

451   the three carriers and the thin coating layers (10 – 15μm) as shown from the μCT analysis.

452   In vivo transdermal delivery of insulin in diabetic mice

453   Diabetes was successfully induced in mice after 7 days of streptozotocin administration. The

454   preliminary diabetes (hyperglycemia) was demonstrated as 340 ± 10 mg/dl. The diabetic mice

455   were divided into three groups: Untreated (negative control), subcutaneously (SC) injected

456   (positive control) and treated with the 3D printed insulin-coated MNs. Fig. 9 shows the

457   application process of the 3D printed MN arrays.

458   The dose 0.2 IU/array was selected in order to avoid hypoglycaemia in mice for 4 h. The

459   comparative studies on different delivery strategies in plasma glucose levels are shown in Fig.

460   10a. Insulin-coated 3D printed MN arrays showed a remarkable steady state hypoglycaemia

461   effect (32.8% from total value) in comparison to negative and positive control. After an hour,

462   subcutaneous injection (0.2 IU/injection) facilitated a rapid increase in insulin concentration in

463   blood and hence the decrease in plasma glucose level was approximately 30.1% from its primary

464   value. A comparable blood glucose regulation was observed between the SC group and the MN

465   group which was achieved within 1 h [51]. Interestingly, the 3D printed patch presented the same

466   rate to reach its lowest glucose level compared to the SC injection. In similar study

467   biodegradable MN patches Tmin of glucose levels was achieved within 2 h with administrated

468   doses of $5 - 10$ IU per patch [13]. The main reason for the faster glucose rates is that in *Zhang et*

469   *al.* (2018) insulin was encapsulated in moulded MN patches while for the 3D printed patches is

470   applied on the microneedle surface with very hydrophilic thin layers resulting in rapid insulin

471   release. Moreover, previous studies have shown that microneedle injection of insulin to human

472   diabetic subjects was chosen over hypodermic infusion and that pharmacokinetics were faster

473   when insulin was administered to the skin compared to the subcutaneous injections [52].

474   Although the plasma glucose level versus time profile was similar to previous findings [53–57]

475   the steady state plasma glucose level was maintained up to 4 h while the untreated group

476 (negative control) remained unchanged (no hypoglycaemia) for the same period. These findings

477 suggest that insulin is being released from the 3D printed MNs to the mice blood stream via

478 passive diffusion to blood capillary.

479 Fig. 10b illustrates the plasma insulin concentration versus time where both SC and 3D printed

480 MN groups achieved the highest amount of plasma insulin concentration after 1 h of

481 administration. The control group did not show any detectable plasma insulin concentration. The

482 highest insulin level of the 3D printed MNs is slightly lower to the SC injection but no statistical

483 difference was observed. As shown in Fig. 10b after post – administration for 4 h the serum

484 insulin of 3D printed microneedles was higher to the SC injection.

485 Tables 2 and 3 represent the pharmacodynamic parameters of plasma glucose levels and the

486 pharmacokinetic parameters for plasma insulin concentrations, respectively. The RPA and RBA

487 for the insulin-coated 3D printed MNs group were both about 85-96%. These results indicate that

488 insulin released from 3D printed MNs was almost completely absorbed from the skin into the

489 systemic circulation, and the pharmacological activity of the released insulin remained intact

490 after the delivery with the 3D printed MNs.

491 Conclusions

492 MN arrays of high quality and reproducibility, featuring spear and pyramid-shaped needle

493 geometries, were successfully fabricated by a biocompatible resin using stereolithography. The

494 3D printed polymeric MNs required low forces to penetrate porcine skin, in comparison with

495 metallic MNs. Uniform and accurate insulin-sugar thin layers were applied on the surface of the

496 MNs through inkjet printing, with no satellite droplets detected on the substrate. The insulin

497 integrity was found to be preserved by all carriers, namely the α–helix and β-Sheet, with xylitol

498   showing the optimum performance. *In vivo* animal trials demonstrated that 3D printed MNs

499   facilitate rapid low glucose levels with longer duration compared to SC injections.

500

502
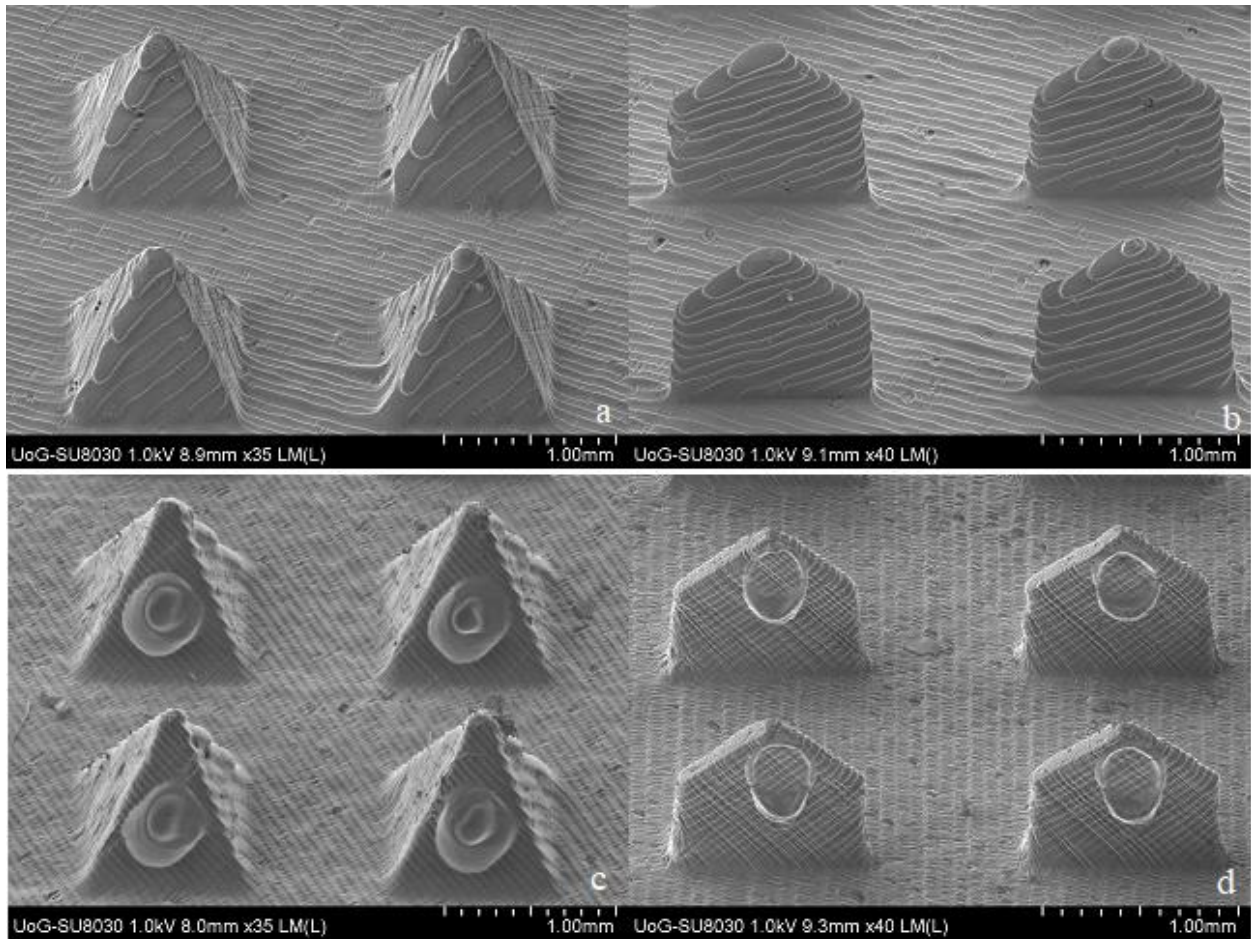
Figure 1. SEM images of the 3D printed MNs. (a) Uncoated pyramid; (b) uncoated spear; (c) coated pyramid; (d) coated spear. The thin coating films on the MNs were created using an inkjet printer. The formulations employed for the coatings contained insulin and a sugar used as a carrier (xylitol, mannitol and trehalose) in a 5:1 ratio. Each MN patch was coated with 10 IU. All insulin-carrier combinations formed coatings with similar morphology. The carrier used for captions (c) and (d) is xylitol.
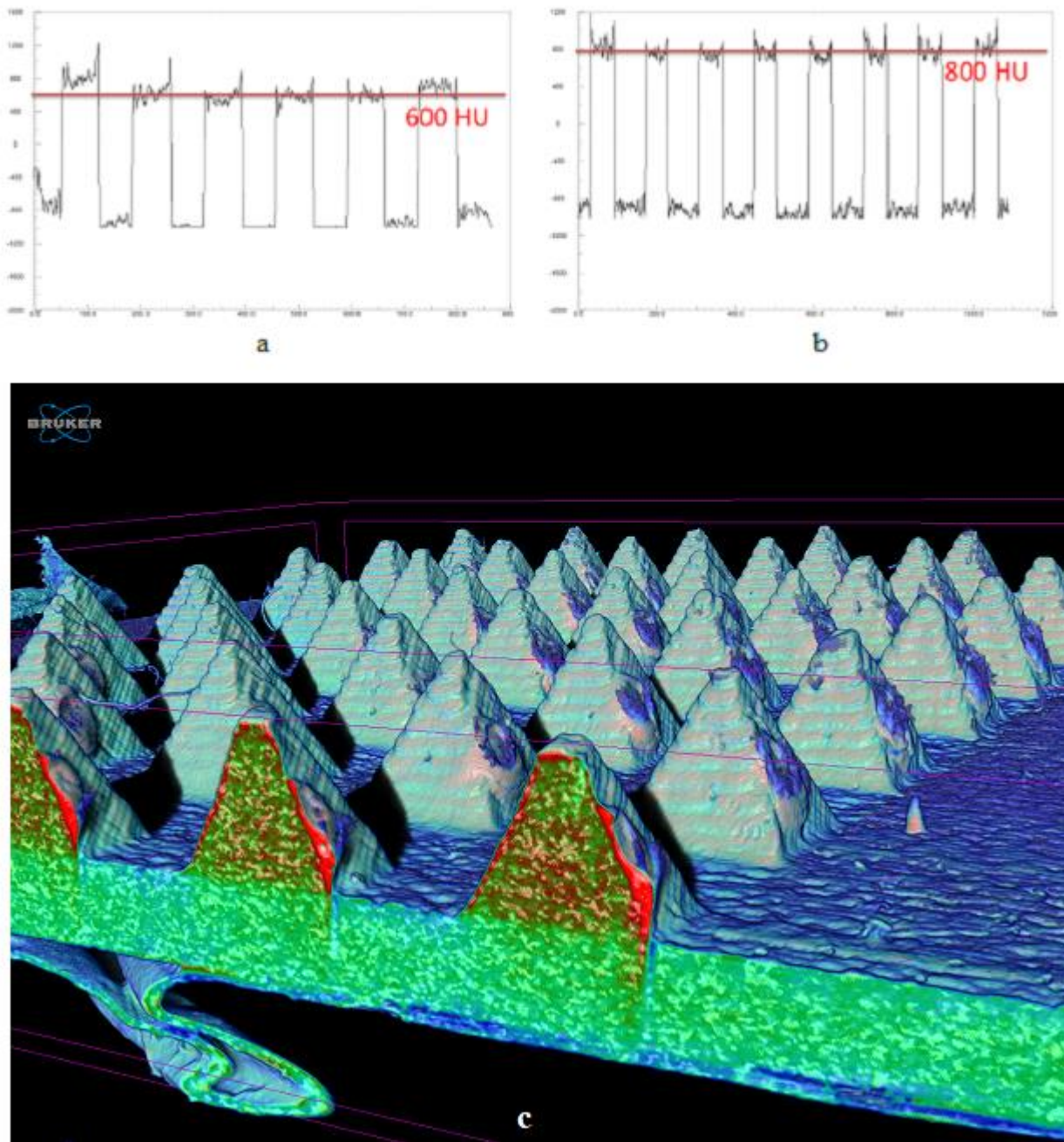
509

510
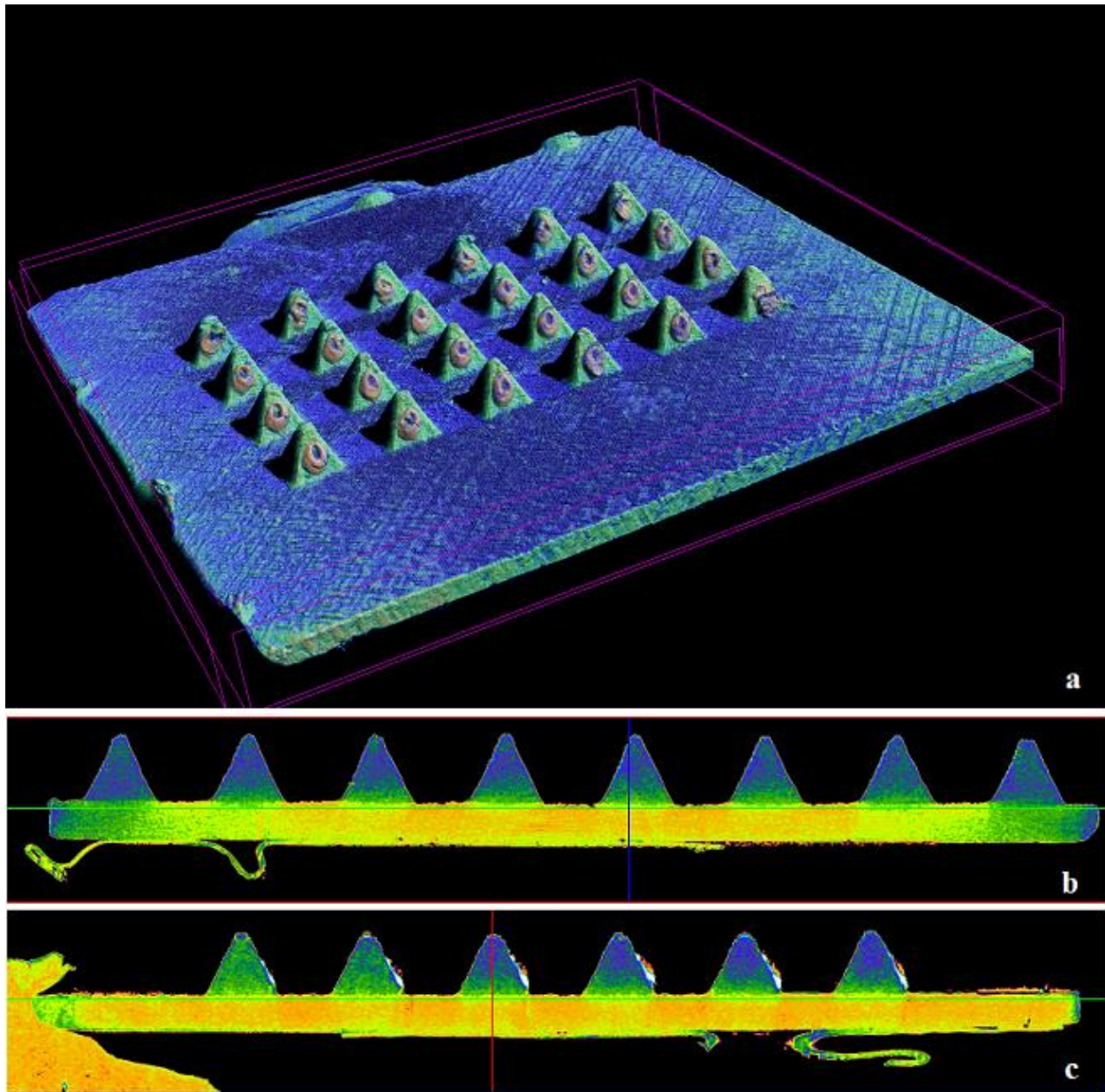
Figure 2. μCT images of the pyramid MN arrays coated with insulin:xylitol formulation.

(a) Overview; (b) image taken from the back side; (c) image taken from the left-hand side of the
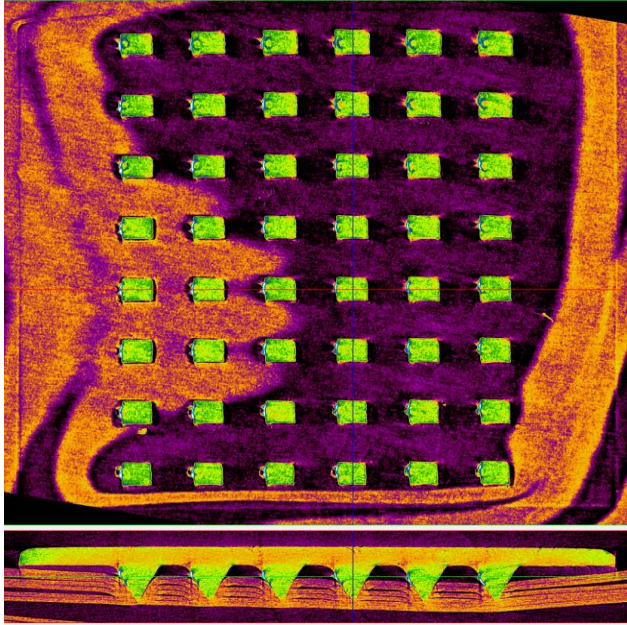
array, showing the thin film coating.

514

Figure 3. μCT evaluation. (a) Profile lines, measured across a single row of the control sample (uncoated array) and (b) the coated pyramid MN array with insulin:xylitol formulation, showing a 200 HU increase; (c) cross-section of the coated MN array showing a fringe layer of 10-15 μm.
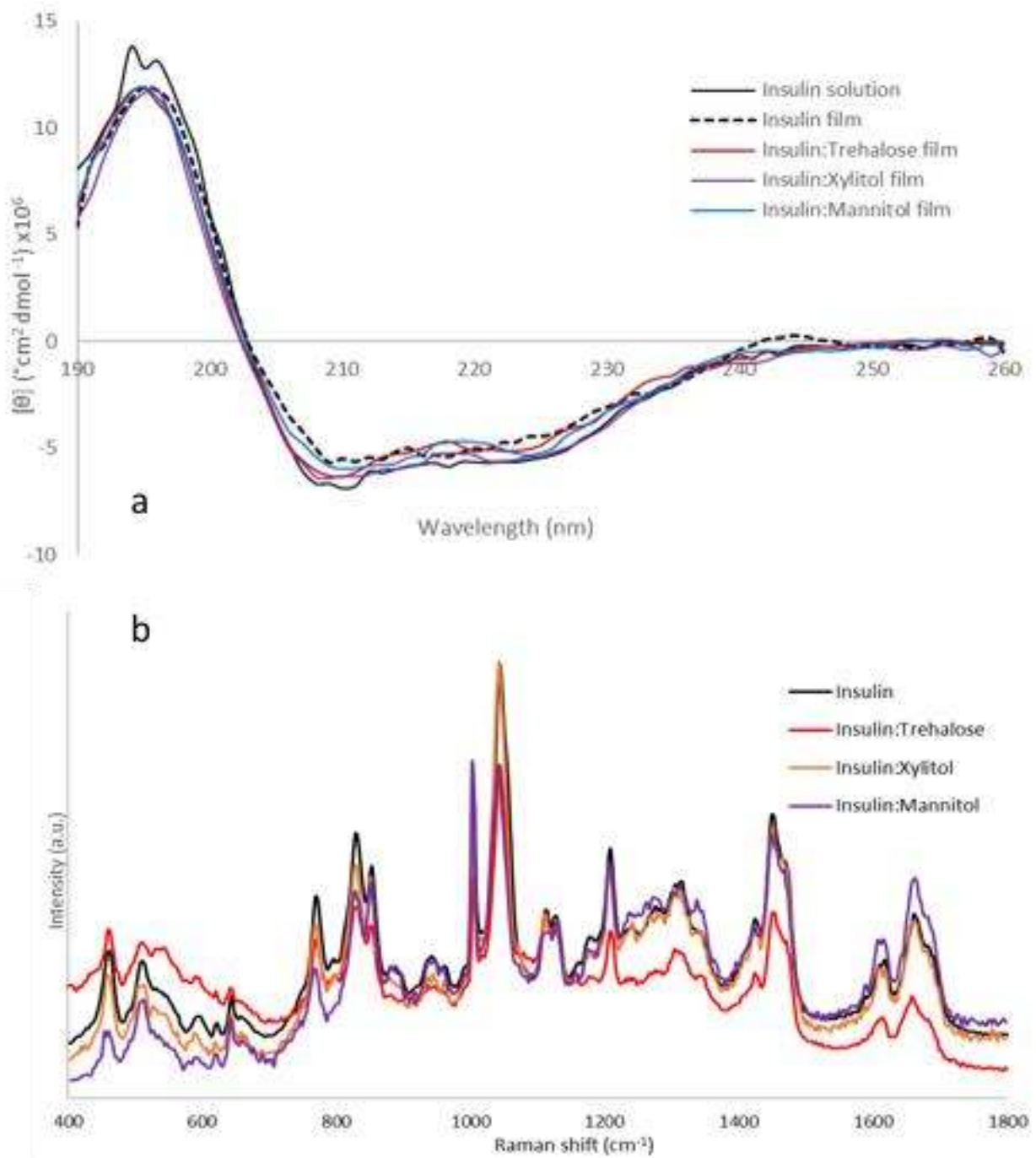
518

519 Figure 4. Cross section of MN array penetration through 8-ply strip of parafilm, applying a 5N
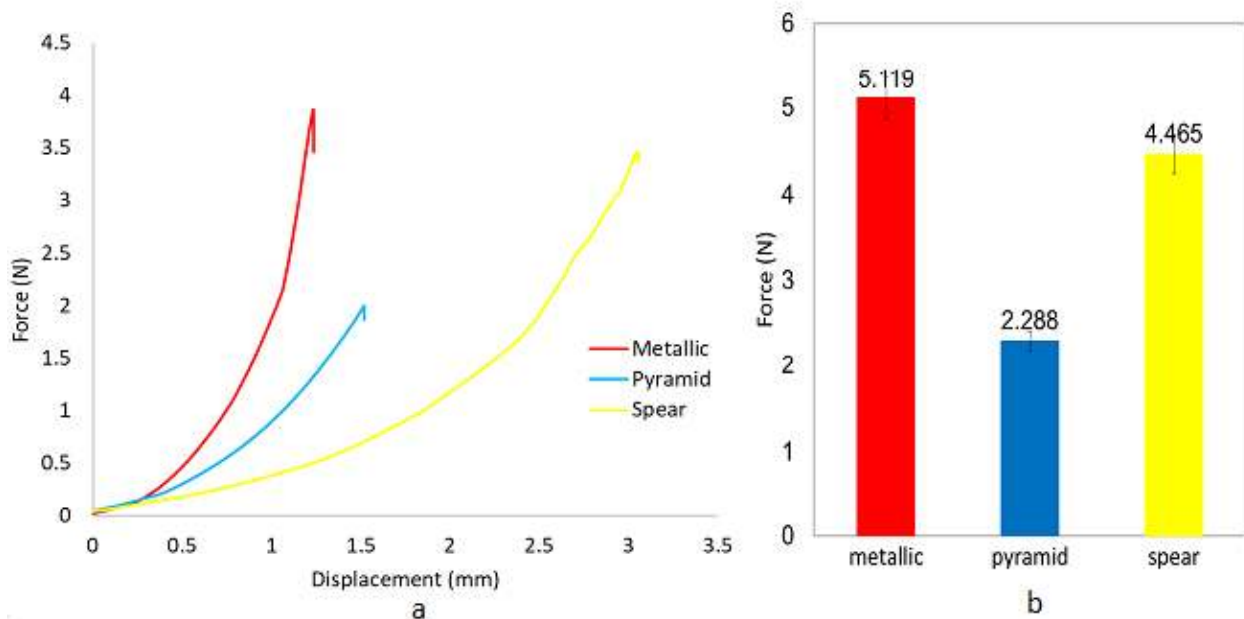520 load.

521

522
523

524

Figure 5. **a)** CD of insulin and insulin formulations and b) Raman spectra from 500 to 1800 cm^{-1} of pure insulin and insulin-sugars.

Figure 6. Penetration studies of MNs through porcine skin, comparing 3D printed spear and pyramid designs with metallic MNs. (a) Force against displacement curves recorded during MN insertion tests; (b) Maximum force required for MN penetration.
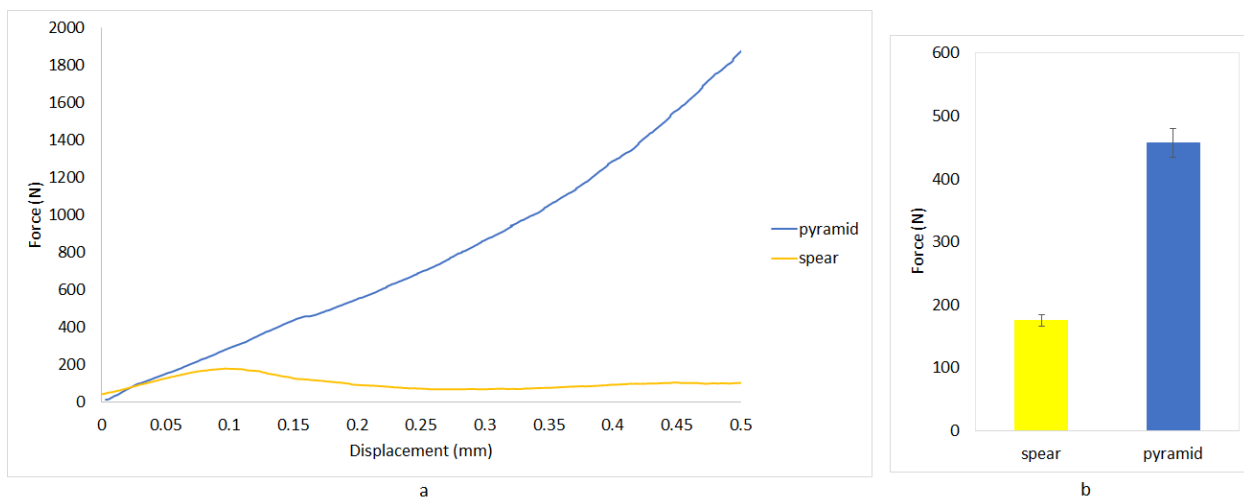
Figure 7. MN fracture testing for pyramid and spear designs. (a) Force against displacement curves recorded during MN fracture tests; (b) Fracture MN strength
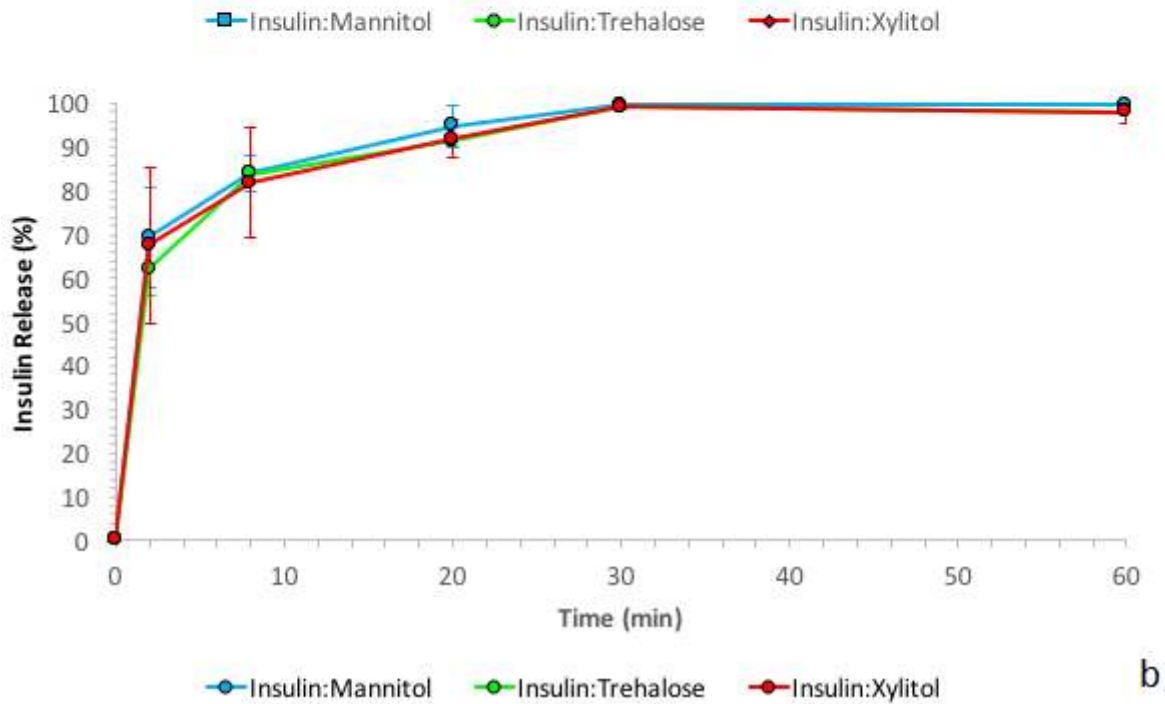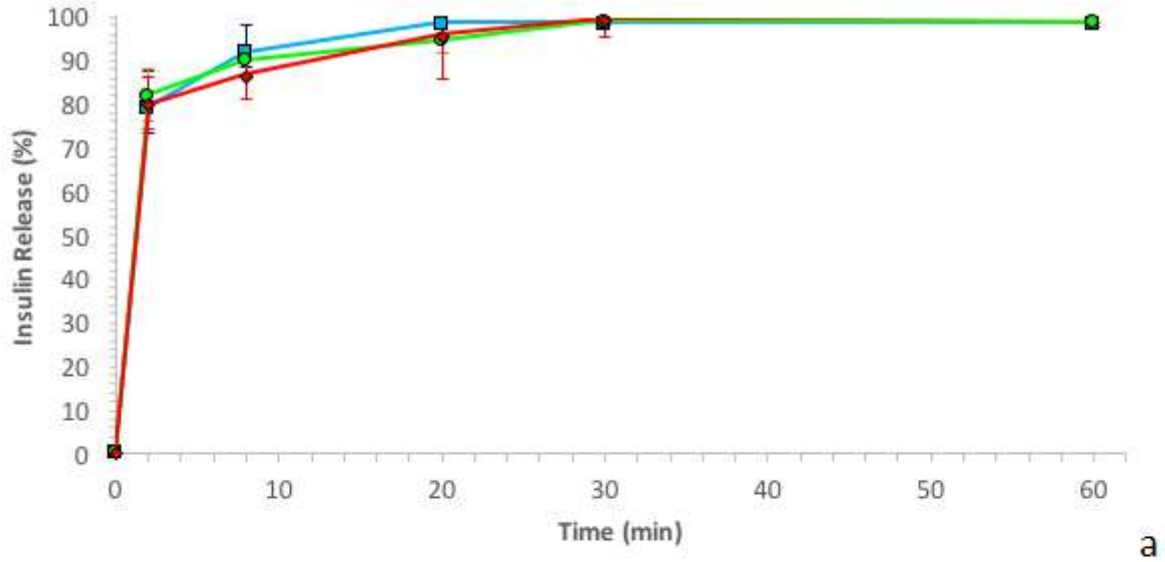
Figure 8. In vitro insulin release through porcine skin from a) the pyramid and b) the spear MN designs for all investigated drug carriers.
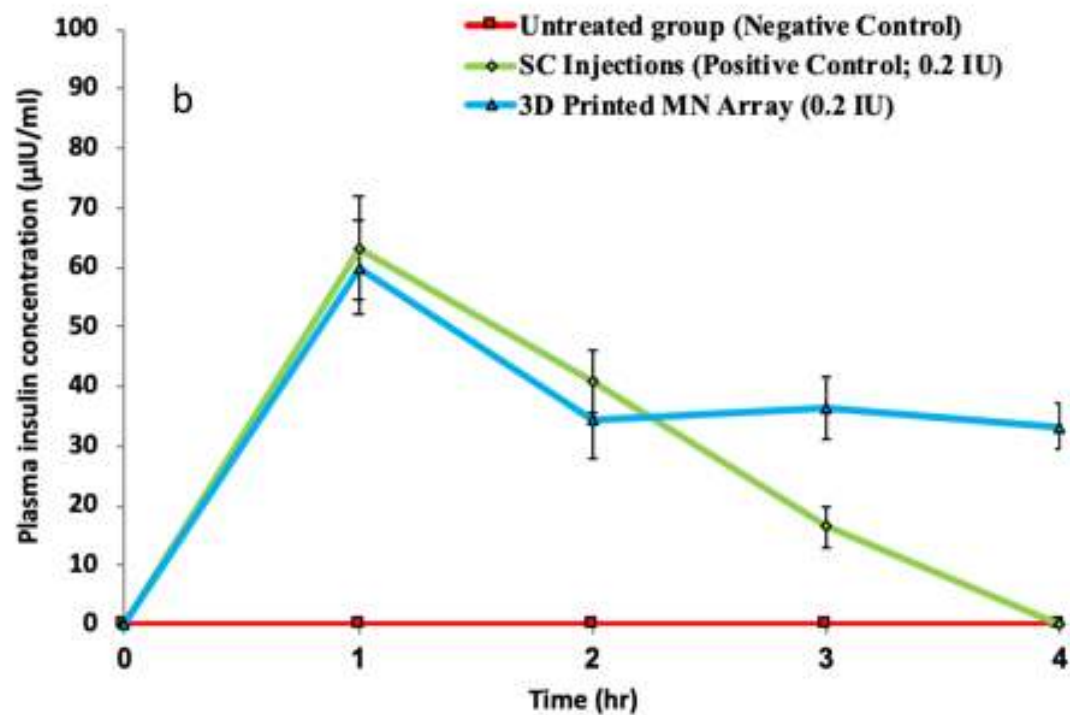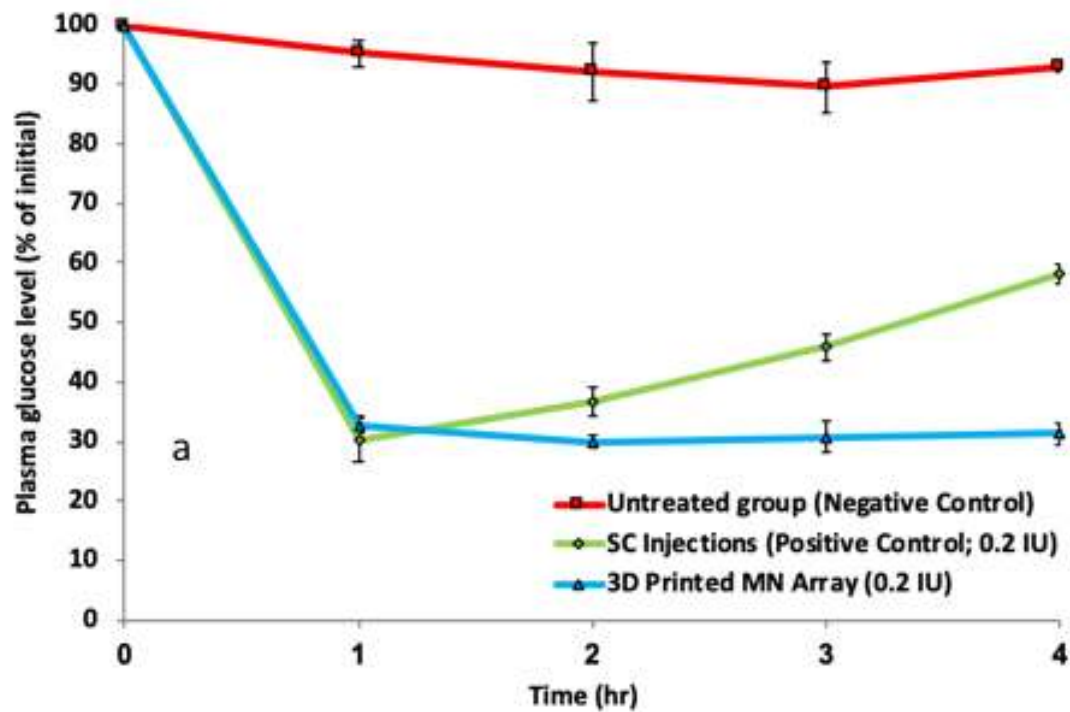
539
540 Figure 9. Experimental mice (A) before the application, (B) during the application and (C) after
541 removal of the 3D printed MN array for the delivery of insulin to diabetic mice.

542

543 Figure 10. a) Comparative plasma glucose level vs time for untreated group, subcutaneous (SC)
544 injection and insulin-coated 3D Printed MN array applied to diabetic mice, over 4 hours (n=3),

545   b) comparative plasma insulin concentration vs time for untreated group, subcutaneous (SC)
546   injection and insulin-coated 3D Printed MN array applied to diabetic mice, over 4 hours (n=3).

547

548   TABLES

549   **Table 1** Treatment protocol for insulin-coated 3D printed MN array.

Day	Stage	Treatment strategy
-7	Animal model selection and isolation	Transfer mice to study isolator
0	Induction of diabetes	• Weigh animals and injected with streptozotocin (diabetes inducer) • Daily blood glucose measurements
1		
2		
3	Observation	Blood glucose level measurements
4		
5		
6		
7	Confirmation of diabetes induction	Blood glucose level exceeds 300 mg/dl within 7 days.
8	Antidiabetic therapy using insulin-coated 3D printed MN array	After treatment, hourly (up to 4 hours) blood samples were collected from the jugular vein and the blood glucose level was measured. The study was conducted for 24 hours.

550

551

552 **Table 2**. Pharmacodynamic parameters for plasma glucose levels of diabetic mice for untreated
553 groups, subcutaneous (SC) injection (insulin dose: 0.2 IU) and 3D Printed MN array (insulin
554 dose: 0.2 IU) (n=3).

Group	C_{min} (%)	T_{min} (h)	$AAC_{0\ to\ 4}$ (% hr)	RPA (%)
Untreated groups	89.5 ± 4.2	3	22.7 ± 1.2	-
SC injections	32.8 ± 3.7	1	208.5 ± 3.7	100
3D Printed MN arrays	30.1 ± 1.0	1	240.6 ± 2.9	122

555 C_{min}, minimum glucose level; T_{min}, time point of minimum glucose level; $AAC_{0\ to\ 4}$, area above
556 the plasma glucose concentration vs. time curve; RPA, relative pharmacological availability
557 compared to subcutaneous injection.

558

559 **Table 3**. Pharmacokinetic parameters for plasma glucose levels of diabetic mice for untreated
560 groups, subcutaneous (SC) injection (insulin dose: 0.2 IU) and 3D Printed MN array (insulin
561 dose: 0.2 IU) (n=3).

Group	C_{max} (μIU ml^{-1})	T_{max} (h)	$AUC_{0\ to\ 4}$ (μIUhr^{-1} ml^{-1})	RBA (%)
Untreated groups	0	0	0	0
SC injections	63.2 ± 8.8	1	120.5 ± 6.4	100
3D Printed MN arrays	59.9 ± 7.9	1	147.4 ± 5.8	115

562 C_{max}, maximum plasma insulin concentration; T_{max}, time point of maximum plasma insulin
563 concentration; $AUC_{0\ to\ 4}$, area under the plasma insulin concentration vs. time curve; RBA,
564 relative bioavailability compared with subcutaneous injection.

565

AUTHOR INFORMATION

Corresponding Authors

* Corresponding Authors: Prof. D.A. Lamprou, E-mail address: d.lamprou@qub.ac.uk, Tel.: +44(0) 2890 97 2617. Prof. D. Douroumis, E-mail: d.douroumis@gre.ac.uk, Tel: +44 (0) 2083 31 8440.

Author Contributions

The manuscript was written through contributions of all authors. All authors have given approval to the final version of the manuscript.

ABBREVIATIONS

Transdermal Drug Delivery, TDD; MN, microneedle; poly(vinyl alcohol), PVA; glucose oxidase, GOx; Additive Manufacturing, AM; UV, ultraviolet; CD, Circular Dichroism; µCT, Micro Computer Tomography; Scanning electron microscopy, (SEM); High-Performance Liquid Chromatography, (HPLC); relative humidity, (RH).

DATA AVAILABILITY

The data will be available on request.

586

587

REFERENCES

589

[1]   A.Z. Alkilani, M.T.C. McCrudden, R.F. Donnelly, Transdermal drug delivery: Innovative pharmaceutical developments based on disruption of the barrier properties of the stratum corneum, Pharmaceutics. 7 (2015) 438–470. doi:10.3390/pharmaceutics7040438.

[2]   W. Chen, H. Li, D. Shi, Z. Liu, W. Yuan, Microneedles As a Delivery System for Gene Therapy, Front. Pharmacolocy. 7 (2016) 137. doi:10.3389/fphar.2016.00137.

[3]   S.T. Sanjay, W. Zhou, M. Dou, H. Tavakoli, L. Ma, F. Xu, X.J. Li, Recent advances of controlled drug delivery using microfluidic platforms, Adv. Drug Deliv. Rev. 128 (2018) 3–28. doi:10.1016/j.addr.2017.09.013.

[4]   L. Goodchild, Could dissolvable microneedles replace injected vaccines?, Mater. Today. 18 (2015) 419–420. doi:10.1016/j.mattod.2015.08.005.

[5]   S. Kaushik, A.H. Hord, D.D. Denson, D. V. McAllister, S. Smitra, M.G. Allen, M.R. Prausnitz, Lack of pain associated with microfabricated microneedles, Anesth. Analg. 92 (2001) 502–504. doi:10.1213/00000539-200102000-00041.

[6]   D.P. Wermeling, S.L. Banks, D.A. Hudson, H.S. Gill, J. Gupta, M.R. Prausnitz, A.L. Stinchcomb, Microneedles permit transdermal delivery of a skin-impermeant medication to humans, Proc. Natl. Acad. Sci. 105 (2008) 2058–2063. doi:10.1073/pnas.0710355105.

[7]   R.F. Donnelly, T.R.R. Singh, M.J. Garland, K. Migalska, R. Majithiya, C.M. McCrudden, P.L. Kole, T.M.T. Mahmood, H.O. McCarthy, A.D. Woolfson, Hydrogel-forming microneedle arrays for enhanced transdermal drug delivery, Adv. Funct. Mater. 22 (2012) 4879–4890. doi:10.1002/adfm.201200864.

610   [8]   M. Korytkowski, L. Niskanen, T. Asakura, FlexPen®: Addressing issues of confidence

611   andconvenience in insulin delivery, Clin. Ther. 27 (2005) S89-100.

612   doi:10.1016/j.clinthera.2005.11.019.

613   [9]   X. Guo, W. Wang, Challenges and recent advances in the subcutaneous delivery of

614   insulin, Expert Opin. Drug Deliv. 14 (2017) 727–734.

615   doi:10.1080/17425247.2016.1232247.

616   [10]   R.J. Narayan, Transdermal delivery of insulin via microneedles, J. Biomed. Nanotechnol.

617   10 (2014) 2244–2260. doi:10.1166/jbn.2014.1976.

618   [11]   J. Wang, Y. Ye, J. Yu, A.R. Kahkoska, X. Zhang, C. Wang, W. Sun, R.D. Corder, Z.

619   Chen, S.A. Khan, J.B. Buse, Z. Gu, Core-Shell Microneedle Gel for Self-Regulated

620   Insulin Delivery, ACS Nano. 12 (2018) 2466–2473. doi:10.1021/acsnano.7b08152.

621   [12]   W. Yu, G. Jiang, Y. Zhang, D. Liu, B. Xu, J. Zhou, Polymer microneedles fabricated from

622   alginate and hyaluronate for transdermal delivery of insulin, Mater. Sci. Eng. C. 80 (2017)

623   187–196. doi:10.1016/j.msec.2017.05.143.

624   [13]   Y. Zhang, G. Jiang, W. Yu, D. Liu, B. Xu, Microneedles fabricated from alginate and

625   maltose for transdermal delivery of insulin on diabetic rats, Mater. Sci. Eng. C. 85 (2018)

626   18–26. doi:https://doi.org/10.1016/j.msec.2017.12.006.

627   [14]   S. Ross, N. Scoutaris, D. Lamprou, D. Mallinson, D. Douroumis, Inkjet printing of insulin

628   microneedles for transdermal delivery, Drug Deliv. Transl. Res. 5 (2015) 451–461.

629   doi:10.1007/s13346-015-0251-1.

630   [15]   R.D. Pedde, B. Mirani, A. Navaei, T. Styan, S. Wong, M. Mehrali, A. Thakur, N.K.

631   Mohtaram, A. Bayati, A. Dolatshahi-Pirouz, M. Nikkhah, S.M. Willerth, M. Akbari,

632   Emerging Biofabrication Strategies for Engineering Complex Tissue Constructs, Adv.

633   Mater. 29 (2017) 1–27. doi:10.1002/adma.201606061.

634   [16]   L.E. Visscher, H.P. Dang, M.A. Knackstedt, D.W. Hutmacher, P.A. Tran, 3D printed

635   Polycaprolactone scaffolds with dual macro-microporosity for applications in local

636   delivery of antibiotics, Mater. Sci. Eng. C. 87 (2018) 78–89.

637   doi:10.1016/j.msec.2018.02.008.

638   [17]   H. Tayebi, Lobat.; Rasoulianboroujeni, Morteza.; Moharamzadeh, Keyvan.; Almela,

639   Thafar.K.D.; Cui, Zhanfeng.; Ye, 3D-printed membrane for guided tissue regeneration,

640   Mater. Sci. Eng. C. 84 (2018) 148–158. doi:doi.org/10.1016/j.msec.2017.11.027.

641   [18]   D. Lam, CXF; Mo, XM; Teoh, SH; Hutmacher, Scaffold development using 3D printing

642   with a starch-based polymer, Mater. Sci. Eng. C. 20 (2002) 49–56.

643   doi:doi.org/10.1016/S0928-4931(02)00012-7.

644   [19]   S.N. Economidou, D.A. Lamprou, D. Douroumis, 3D printing applications for transdermal

645   drug delivery, Int. J. Pharm. 544 (2018) 415–424. doi:10.1016/j.ijpharm.2018.01.031.

646   [20]   B. Thavornyutikarn, P. Tesavibul, K. Sitthiseripratip, N. Chatarapanich, B. Feltis, P.F.A.

647   Wright, T.W. Turney, Porous 45S5 Bioglass®-based scaffolds using stereolithography:

648   Effect of partial pre-sintering on structural and mechanical properties of scaffolds, Mater.

649   Sci. Eng. C. 75 (2017) 1281–1288. doi:10.1016/j.msec.2017.03.001.

650   [21]   D. Pede, G. Serra, D. De Rossi, Microfabrication of conducting polymer devices by ink-

651   jet stereolithography, Mater. Sci. Eng. C. 5 (1998) 289–291. doi:10.1016/S0928-

652   4931(97)00056-8.

653   [22]   E.J. Mott, M. Busso, X. Luo, C. Dolder, M.O. Wang, J.P. Fisher, D. Dean, Digital

654   micromirror device (DMD)-based 3D printing of poly(propylene fumarate) scaffolds,

655   Mater. Sci. Eng. C. 61 (2016) 301–311. doi:10.1016/j.msec.2015.11.071.

656 [23] S.D. Gittard, P.R. Miller, C. Jin, T.N. Martin, R.D. Boehm, B.J. Chisholm, S.J. Stafslien,

657 J.W. Daniels, N. Cilz, N.A. Monteiro-Riviere, A. Nasir, R.J. Narayan, Deposition of

658 antimicrobial coatings on microstereolithography-fabricated microneedles, Jom. 63 (2011)

659 59–68. doi:10.1007/s11837-011-0093-3.

660 [24] Y. Lu, S.N. Mantha, D.C. Crowder, S. Chinchilla, K.N. Shah, Y.H. Yun, R.B. Wicker,

661 J.W. Choi, Microstereolithography and characterization of poly(propylene fumarate)-

662 based drug-loaded microneedle arrays, Biofabrication. 7 (2015) 1–13. doi:10.1088/1758-

663 5090/7/4/045001.

664 [25] N. Sreerama, R.W. Woody, Estimation of protein secondary structure from circular

665 dichroism spectra: Comparison of CONTIN, SELCON, and CDSSTR methods with an

666 expanded reference set, Anal. Biochem. 287 (2000) 252–260.

667 doi:10.1006/abio.2000.4880.

668 [26] S.P. Davis, B.J. Landis, Z.H. Adams, M.G. Allen, M.R. Prausnitz, Insertion of

669 microneedles into skin: Measurement and prediction of insertion force and needle fracture

670 force, J. Biomech. 37 (2004) 1155–1163. doi:10.1016/j.jbiomech.2003.12.010.

671 [27] M.J. Uddin, N. Scoutaris, P. Klepetsanis, B. Chowdhry, M.R. Prausnitz, D. Douroumis,

672 Inkjet printing of transdermal microneedles for the delivery of anticancer agents, Int. J.

673 Pharm. 494 (2015) 593–602. doi:10.1016/j.ijpharm.2015.01.038.

674 [28] Z. Yong, D. Yingjie, W. Xueli, X. Jinghua, L. Zhengqiang, Conformational and

675 bioactivity analysis of insulin: Freeze-drying TBA/water co-solvent system in the

676 presence of surfactant and sugar, Int. J. Pharm. 371 (2009) 71–81.

677 doi:10.1016/j.ijpharm.2008.12.018.

678 [29] Y.H. Kim, C. Sioutas, K.S. Shing, Influence of stabilizers on the physicochemical

679   characteristics of inhaled insulin powders produced by supercritical antisolvent process,

680   Pharm. Res. 26 (2009) 61–71. doi:10.1007/s11095-008-9708-y.

681   [30] H. Schiffter, J. Condliffe, S. Vonhoff, Spray-freeze-drying of nanosuspensions: the

682   manufacture of insulin particles for needle-free ballistic powder delivery, J. R. Soc.

683   Interface. 7 (2010) S483-500. doi:10.1098/rsif.2010.0114.focus.

684   [31] L. Whitmore, B.A. Wallace, DICHROWEB, an online server for protein secondary

685   structure analyses from circular dichroism spectroscopic data, Nucleic Acids Res. 32

686   (2004) 668–673. doi:10.1093/nar/gkh371.

687   [32] L. Whitmore, B.A. Wallace, Protein secondary structure analyses from circular dichroism

688   spectroscopy: Methods and reference databases, Biopolymers. 89 (2008) 392–400.

689   doi:10.1002/bip.20853.

690   [33] M.J. Ettinger, S.N. Timasheff, Optical activity of insulin. II. Effect of nonaqueous

691   solvents, Biochemistry. 10 (1971) 831–840.

692   http://www.ncbi.nlm.nih.gov/entrez/query.fcgi?cmd=Retrieve&db=PubMed&dopt=Citati

693   on&list_uids=5544674.

694   [34] B. Sarmento, D.C. Ferreira, L. Jorgensen, M. van de Weert, Probing insulin's secondary

695   structure after entrapment into alginate/chitosan nanoparticles, Eur. J. Pharm. Biopharm.

696   65 (2007) 10–17. doi:10.1016/j.ejpb.2006.09.005.

697   [35] F. Andrade, P. Fonte, M. Oliva, M. Videira, D. Ferreira, B. Sarmento, Solid state

698   formulations composed by amphiphilic polymers for delivery of proteins: characterization

699   and stability, Int. J. Pharm. 486 (2015) 195–206. doi:10.1016/j.ijpharm.2015.03.050.

700   [36] W. Dzwolak, R. Ravindra, J. Lendermann, R. Winter, Aggregation of bovine insulin

701   probed by DSC/PPC calorimetry and FTIR spectroscopy, Biochemistry. 42 (2003) 11347–

702   11355. doi:10.1021/bi034879h.

703   [37]   J.F. Carpenter, J.H. Crowe, An infrared spectroscopic study of the interactions of

704   carbohydrates with dried proteins, Biochemistry. 28 (1989) 3916–3922.

705   doi:10.1021/bi00435a044.

706   [38]   M.A. Haque, J. Chen, P. Aldred, B. Adhikari, Drying and denaturation characteristics of

707   whey protein isolate in the presence of lactose and trehalose, Food Chem. 177 (2015) 8–

708   16. doi:10.1016/j.foodchem.2014.12.064.

709   [39]   S.G. Melberg, W.C. Johnson, Changes in secondary structure follow the dissociation of

710   human insulin hexamers: A circular dichroism study, Proteins Struct. Funct. Bioinforma. 8

711   (1990) 280–286. doi:10.1002/prot.340080309.

712   [40]   D.C.O. Nai-Teng Yu, C.S. Liu, Laser Raman Spectroscopy and the Conformation and

713   Proinsulin of Insulin, J. Mol. Biol. 70 (1972) 117–132.

714   [41]   P.O. Souillac, C.R. Middaugh, J.H. Rytting, Investigation of protein / carbohydrate

715   interactions in the dried state . 2 . Diffuse reflectance FTIR studies, Int. J. Pharm. 235

716   (2002) 207–218.

717   [42]   A. Das, P. Basak, R. Pattanayak, T. Kar, R. Majumder, D. Pal, A. Bhattacharya, M.

718   Bhattacharyya, S.P. Banik, Trehalose induced structural modulation of Bovine Serum

719   Albumin at ambient temperature, Int. J. Biol. Macromol. 105 (2017) 645–655.

720   doi:10.1016/j.ijbiomac.2017.07.074.

721   [43]   J. Lee, S. Timasheff, The Stabilization of Proteins by Sucrose *, J. Biol. Chem. 256

722   (1981) 7193–7201.

723   [44]   S. Yoshioka, T. Miyazaki, Y. Aso, b-Relaxation of Insulin Molecule in Lyophilized

724   Formulations Containing Trehalose or Dextran As a Determinant of Chemical Reactivity,

725   Pharm. Res. 23 (2006) 961–966. doi:10.1007/s11095-006-9907-3.

726 [45] C. Branca, S. MacCarrone, S. Magazu, G. Maisano, S.M. Bennington, J. Taylor,

727   Tetrahedral order in homologous disaccharide-water mixtures, J. Chem. Phys. 122 (2005)

728   174513-1-174513–6. doi:10.1063/1.1887167.

729 [46] N.K. Jain, I. Roy, Effect of trehalose on protein structure, Protein Sci. 18 (2009) 24–36.

730   doi:10.1002/pro.3.

731 [47] G. Zeng, J.J. Shou, K.K. Li, Y.H. Zhang, In-situ confocal Raman observation of structural

732   changes of insulin crystals in sequential dehydration process, Biochim. Biophys. Acta -

733   Proteins Proteomics. 1814 (2011) 1631–1640. doi:10.1016/j.bbapap.2011.09.002.

734 [48] L.G. Tensmeyer, J.E. Shields, E. Lilly, The Raman Spectra of Crystalline 4Zn, 2Zn, and

735   Na Insulin., 1336 (1990) 222–234.

736 [49] H. Takeuchi, N. Watanabe, Y. Satoh, I. Harada, Effects of Hydrogen Bonding on the

737   Tyrosine Raman Bands in the 1300-1150 cm - Region, 20 (1989) 233–237.

738 [50] S.D. Gittard, B. Chen, H. Xu, A. Ovsianikov, B.N. Chichkov, N.A. Monteiro-Riviere, R.J.

739   Narayan, The effects of geometry on skin penetration and failure of polymer

740   microneedles, J. Adhes. Sci. Technol. 27 (2013) 227–243.

741   doi:10.1080/01694243.2012.705101.

742 [51] I.C. Lee, Y.C. Wu, S.W. Tsai, C.H. Chen, M.H. Wu, Fabrication of two-layer dissolving

743   polyvinylpyrrolidone microneedles with different molecular weights for: In vivo insulin

744   transdermal delivery, RSC Adv. 7 (2017) 5067–5075. doi:10.1039/c6ra27476e.

745 [52] J. Gupta, S.S. Park, B. Bondy, E.I. Felner, M.R. Prausnitz, Infusion pressure and pain

746   during microneedle injection into skin of human subjects, Biomaterials. 32 (2011) 6823–

747   6831. doi:10.1016/j.biomaterials.2011.05.061.

748   [53]   M. Ling, M. Chen, Dissolving polymer microneedle patches for rapid and efficient

749   transdermal delivery of insulin to diabetic rats., Acta Biomater. 9 (2013) 8952–8961.

750   doi:10.1016/j.actbio.2013.06.029.

751   [54]   S. Liu, M. Jin, Y. Quan, F. Kamiyama, H. Katsumi, T. Sakane, A. Yamamoto, The

752   development and characteristics of novel microneedle arrays fabricated from hyaluronic

753   acid, and their application in the transdermal delivery of insulin., J. Control. Release. 161

754   (2012) 933–41. doi:10.1016/j.jconrel.2012.05.030.

755   [55]   S. Fakhraei Lahiji, Y. Jang, I. Huh, H. Yang, M. Jang, H. Jung, Exendin-4-encapsulated

756   dissolving microneedle arrays for efficient treatment of type 2 diabetes, Sci. Rep. 8 (2018)

757   1–9. doi:10.1038/s41598-018-19789-x.

758   [56]   Y. Qiu, G. Qin, S. Zhang, Y. Wu, B. Xu, Y. Gao, Novel lyophilized hydrogel patches for

759   convenient and effective administration of microneedle-mediated insulin delivery, Int. J.

760   Pharm. 437 (2012) 51–56. doi:10.1016/j.ijpharm.2012.07.035.

761   [57]   S.P. Davis, W. Martanto, M.G. Allen, S. Member, M.R. Prausnitz, Hollow Metal

762   Microneedles for Insulin Delivery to Diabetic Rats, 52 (2005) 909–915.

763